An advanced immersed fluid-structure interaction particle method for cardiovascular applications experimentally validated versus a new benchmark case

Alessandra Monteleone[1*], Sofia Di Leonardo[1*], Marco Correnti[1,2], Enrico Napoli[2], Giorgio Micale[2] and Gaetano Burriesci[1,2,3✉]

[1]Ri.MED Foundation, Palermo, Italy
[2]Engineering Department, University of Palermo, Italy
[3]UCL Mechanical Engineering, University College London, UK

[*]Contributed equally
✉ Corresponding author (Address: Viale delle Scienze, Ed. 8 • 90128, Palermo, Italy, Room 1200, Telephone: +39 091 2389 7251, Email: gaetano.burriesci@unipa.it)

Abstract

Fluid-structure interaction (FSI) is crucial in the numerical simulation of cardiovascular phenomena, where pulsatile blood flow dynamically interacts with highly deformable tissues. High-fidelity FSI approaches have become essential to enhance the understanding of potentially lethal pathologies, assisting diagnosis and development of novel therapeutic solutions. This work presents and experimentally validates a new totally meshless FSI approach, specifically designed for cardiovascular applications.

The method is based on the Lagrangian smoothed particle hydrodynamics (SPH), employing a unified physics to represent both blood and deformable walls, avoiding FSI interfaces. A key advantage of this FSI method lies in its ability to overcome the SPH complex issue in contour management, a common challenge that typically increases the complexity of this methodology in FSI applications. Deformable walls are immersed in the fluid domain, and a buffer region of fluid is defined to handle the structural deformation.

For validation, a new FSI benchmark is proposed and analysed with the particle image velocimetry technique. Tailored to entail the typical complexities of relevant cardiovascular situations, the benchmark involves pulsatile flow interacting with a chamber with deformable curved walls, moving through both filling and emptying phases. Despite its simplified geometry, designed to allow a reliable experimental validation, the structure experiences a field of three-dimensional strains and large volume variations, thereby replicating complexities often associated with more intricate models.

Numerical and experimental results show good agreement in terms of fluid velocity field and structural deformation, establishing the proposed totally meshless FSI approach as a reliable tool for complex cardiovascular modelling.

Keywords

Fluid-structure interaction (FSI); Smoothed particle hydrodynamics (SPH); Particle-image velocimetry (PIV); FSI benchmark; Cardiovascular numerical simulation

1. Introduction

Fluid-structure interaction (FSI) is a pivotal and ubiquitous mechanism in various technological fields, particularly in cardiovascular bioengineering [1–3]. In the cardiocirculatory system, pulsatile

blood flows dynamically interact with highly deformable tissues, such as vessel walls, heart chambers and valves. Recognising that cardiovascular diseases are the leading cause of global morbidity and mortality [4], accurate simulation of cardiovascular FSIs has become a priority in biomechanics [1,5]. In this scenario, thanks to the increase in computational power and availability of resources [6], numerical FSI methods are becoming fundamental tools aimed at improving the understanding of physiological phenomena [7], assisting the diagnosis of cardiovascular pathologies [8,9], as well as lead the development and optimisation of medical devices and treatments [10,11]. Numerical FSI methods have been widely used to investigate the haemodynamics of native (healthy and pathological) [7,12–14] and artificial heart valves [15–20], coronary arteries [21,22], the progression of conditions like atherosclerosis [23–25], aortic dissections [26], abdominal aortic aneurysm [27–29] and cerebral aneurysm [30–33]. Furthermore, FSI approaches have been employed for assessing the blood stasis and the associated potential thromboembolic risk in the left atrial appendage (LAA) [8,34].

In FSI simulations, computational fluid and structural dynamics (CFD and CSD, respectively) are coupled using partitioned or monolithic approaches [35–37]. In the former, fluid and structural computational domains are solved separately and the solutions are then matched using one-way (weak coupling, only fluid influences structural results, or *viceversa*) or two-way schemes (strong coupling, fluid and structure affect each other) [38]. On the other hand, in monolithic FSI, a single system of equations is used to solve simultaneously fluid and structural domains [39].

Conventional FSI approaches typically employ grid-based methods, coupling a Eulerian formulation for the fluid domain based on the finite volume method (FVM) with a Lagrangian formulation for the structural domain, generally based on the finite element method (FEM). The interaction between the two computational domains is handled with suitable algorithms, among which the most used in cardiovascular FSI simulations are the arbitrary Lagrangian Eulerian (ALE) [40–42] and the immersed boundary (IB) [43–46]. The ALE approach, implemented both in partitioned or monolithic FSI schemes, employs a boundary fitted mesh that moves with a smoothed and arbitrary velocity [1,47]. The main drawback of ALE is the need for a continuous update of the mesh and boundary conditions, which leads to heavy computational efforts [48,49]. The IB method, firstly introduced by Peskin [50] to simulate the haemodynamics of heart valves, avoids the mesh regeneration issue of ALE, and are therefore more efficient in applications characterised by large deformations [45]. The method, typically implemented in partitioned FSI schemes, uses a fixed mesh for the fluid domain and a deformable mesh for the structure. Overlapping regions between fluid and structural domains are identified and a force term is added in the fluid equations to deal with the presence of the structure. Both ALE and IB coupling techniques encounter difficulties in the modelling of phenomena where the domain separates into unconnected regions, such as that occurring with the closing of heart or vascular valves [51–53].

Alternative FSI strategies are based on meshless numerical methods [54]. Among these, smoothed particle hydrodynamics (SPH) stands out [55–58]. This Lagrangian particle-based method was first proposed by Lucy [59] and Gingold & Monahan [60] to simulate interstellar flows, and afterwards applied in various fields of engineering and science [61,62]. In FSI modelling, SPH was combined with FEM [63–65], or other approaches such as the element bending group method [66,67], the smoothed point interpolation method [68] or particle–spring systems [69]. Other FSI approaches were proposed, where SPH is employed to describe both fluid and solid domains, using the weakly-compressible (WCSPH) [55,70] and the truly incompressible (ISPH) [71,72] techniques. In 2024, Monteleone *et al.* [73] proposed a mono-physics FSI approach fully integrated in the ISPH scheme,

where a single algorithm and physics are employed to solve fluid and structural domains. The mono-physics FSI method is especially suited for cardiovascular problems, where structures typically consist of biological soft tissues, and exhibit incompressibility and similar density to blood [51,74–77]. Moreover, it offers significant advantages over traditional FSI strategies for biological valve modelling, enabling complete valve coaption with no need for remeshing or complex FSI interface management. In previous studies, this method was successfully applied to model the dynamics of the aortic valve leaflets, describing the aortic wall as a rigid boundary [73]. In the context of thrombus formation modelling, the same research group [78] also implemented a similar FSI approach, where the structural domain is not predefined (as in [73]), but it is dynamically generated to model the formation and growth of blood clots. This approach was recently used in Lo Presti *et al.* [79] to model thrombus formation, growth, and embolisation within the LAA, imposing to the chamber walls a prescribed motion modelling atrial fibrillation dynamics. This, necessarily neglects the dynamic changes in the wall velocity caused by the thrombus presence as it forms, thus overlooking the direct interaction between the LAA tissue and the blood flow.

In the present work, the mono-physics FSI approach [73] is extended to the modelling of deformable walls. Both fluid and structural domains are represented with SPH particles, with springs links added between the particles belonging to the solid domain to describe the structural response. The solid domain is immersed in the fluid domain, which includes a buffer volume larger than the region expected to be enveloped by the structure during its motion. Three types of particles are thus defined, depending on the region to which they belong: *effective fluid* particles (inside the fluid domain), *solid* particles (in the structural domain) and *reservoir fluid* particles (in the buffer region). The latter are free to enter in/leave the computational domain through open boundaries, employing the procedure described in Monteleone *et al.* [80]. Each particle interacts with its neighbouring, independently of their type, following the ISPH formulation. This FSI approach is fully meshless, as it does not require the definition of FSI interfaces, whose handling represents a very challenging task for computational methods [2].

This method is here validated versus a new benchmark test specifically designed to simulate relevant challenges in cardiovascular problems. Specifically, a structure made from a highly deformable incompressible material is subjected to a pulsatile fluid flow, while ensuring straightforward experimental replication and analysis. The structure geometry can be regarded as an idealisation of common anatomical structures such as the LAA or an aneurysm, allowing for relevant, although simplified, FSI studies in complex cardiovascular settings. Experimental tests are analysed using particle image velocimetry (PIV), which is a gold standard in experimental flow characterisation [1,81,82] and is widely used for the validation of numerical simulations [7,83–85]. Reference data of the recommended benchmark (geometry and boundary conditions), alongside numerical and experimental results (in terms of flow velocity and structural deformation) are provided to support validation of other computational FSI methods in this field.

2. Methods

2.1. Numerical method

A mono-physics FSI approach [73] is adopted in this study, integrated into the PANORMUS (PArallel Numerical Open-souRce Model for Unsteady flow Simulations) software [86]. The following section provides a concise overview of the methodology, specifically highlighting its novel

application, as presented in the current work, for modelling the interaction between deformable walls and pulsatile flows. The governing equations and numerical formulation are described only to the extent necessary to understand the FSI treatment, particle-based structural modeling, and experimental validation aspects. For the comprehensive mathematical details and derivation of the ISPH scheme, the reader is referred to [73].

Based on the meshless SPH, the approach represents both fluid and solid computational domains with a set of particles. Adhering to the Lagrangian formulation, in SPH the particles move transporting their properties. The field variables at each particle are calculated through discrete convolution integrals with filter functions, named *kernel functions* (W), that are characterised by a specific length h (noted as *smoothing length*) and constant k. The length controls the influence domain of each i particle, including all the neighbouring particles j having a distance from i less than kh. Therefore, a generic function φ at particle i located at position $\mathbf{x}_i$ can be obtained by interpolating the values of the neighbouring particles j:

$$\varphi_i = \sum_{j=1}^{N_i} \frac{m_j}{\rho_j} \varphi_j W_{ij}\,; \tag{1}$$

where N_i is the total number of j particles neighbour to i, m_j and ρ_j represent mass and density of j and $W_{ij} = W(\boldsymbol{x}_i - \boldsymbol{x}_j, h)$.

Governing equations, consisting in momentum and continuity equations for incompressible fluids, are solved employing an incompressible SPH (ISPH) algorithm. The numerical scheme, which follows the fractional-step technique of Chorin [87], is based on predictor-corrector steps as detailed in Monteleone *et al.* [80,88]. In the predictor-step, the momentum equation is firstly solved neglecting the pressure gradient term, to obtain an intermediate non solenoidal velocity. Following, in the corrector-step, a pressure correction is applied to enforce incompressibility, adjusting the predicted velocities to ensure mass conservation. The pressure field is determined implicitly by solving a system of pressure Poisson equations using the BiConjugate Gradient Stabilized method [89].

The mirror particle procedure [86] is used at solid fixed walls to impose suitable boundary conditions and to overcome the truncation of the *kernel function*, while the technique proposed by Monteleone *et al.* [80] is used at the open boundaries.

Furthermore, the shifting procedure proposed by Xu *et al.* [90] is used to maintain a more uniform particle distribution during computation, reducing the well-known *tensile instability* issue [91–93], which leads to particle clustering/blowing away. This procedure consists of shifting slightly the particles across streamlines, allowing an ordered particle distribution to be maintained over time. The values of the hydrodynamic variables are thus adjusted at the new position through a Taylor series expansion. It should be note that, the procedure of Xu *et al.* [90] is applied only to fluid particles, without introducing further stabilisation algorithms for the structural model when large deformation occurs.

In the proposed approach, fluid and solid particles share the same numerical nature and are treated within a unified ISPH framework, whereby a single system of equations is solved for both domains. The interaction between the fluid and the deformable walls is managed through an immersed formulation. Specifically, a computational domain is defined in which the deformable structures are directly embedded within the fluid, eliminating the need for explicit fluid–solid interface tracking. Within this immersed scheme, the fluid region surrounding the structure, referred to as the *buffer volume*, accommodates structural deformation. Owing to the absence of explicitly defined FSI

interfaces, the method is fully meshless, both in the discretisation of the two media and in their coupling. This feature circumvents a well-known limitation of partitioned FSI approaches, in which accurate treatment of the fluid–solid interface is required to ensure consistent and stable matching of the solutions across the two domains.

The method is three-dimensional and allows to handle complex geometries. For the clarity of representation, Figure 1 illustrates a very simple 2D sketch considering a reference state (Figure 1a) and a general deformed configuration (Figure 1b). As first step, the whole computational domain is discretised with SPH particles that are categorised into three groups, depending on the domain in which they fall in the starting configuration. Particles lying inside the structural domain (whose boundaries are indicated with red lines in Figure 1) are identified as *solid* (red circles in Figure 1) and spring links are introduced among them. It should be noted that the boundaries of the structural domain serve only at the beginning, to identify *solid* particles in the reference configuration (Figure 1a). Subsequently, they evolve with the *solid* particle movement without requiring an explicit definition of their position (in Figure 1b, the deformed structural domain are sketched as dashed red lines only for clarity of representation). Particles laying either inside the fluid or in the buffer regions are defined as *effective fluid* (blue circles) or *reservoir fluid* (grey circles), respectively. *Reservoir fluid* particles define a computational region of interest (CRoI) that accommodate for the structural deformation and can enter and leave the computational domain through open boundaries (dotted lines) following the procedure described in Monteleone *et al.* [80].

Particles interact with their neighbours, including those of different types, following the SPH formulation (eq. 1). For instance, Figure 1 highlights the support domain Ω of three particles (i_1, i_2, i_3): Ω_1 contains only *effective fluid* particles, Ω_2 encompasses both *effective fluid* and *solid*, Ω_3 includes both *solid* and *reservoir fluid* particles. It should be noted that, thanks to the absence of FSI interfaces, the current method is entirely meshless both in the treatment of the two media and in their coupling. Therefore, ghost particles are not required to handle fluid–solid interactions.

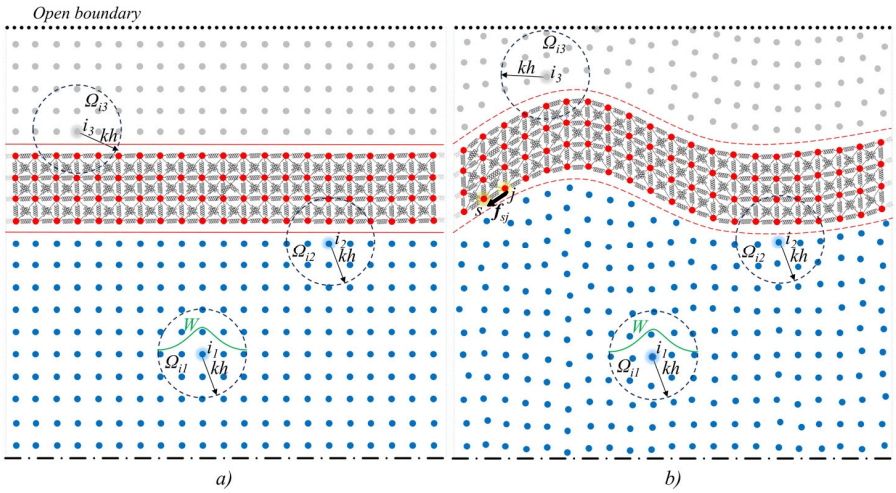

Figure 1: 2D sketch of the immersed FSI numerical method in the reference (a) and deformed (b) configurations. Blue dots: effective fluid particles; red dots: solid particles; grey dots: reservoir fluid particles; dotted line: open boundary; red lines: reference (solid) and virtual deformed (dashed) structural boundaries.

Springs connecting *solid* particles can be stretched or compressed, generating internal elastic forces that attempt to restore their resting length. In Figure 1b, the force $\boldsymbol{f}_{sj}$ between the *solid* particles s and j is indicated. The total internal force per unit mass, $\boldsymbol{f}_s$, on each *solid* particle s can be expressed as vector sum of the forces from all spring couplings it forms with its neighbours.

$$\boldsymbol{f}_s = \frac{k_e\, h}{m_s} \sum_{j=1}^{N_s} \left(d_{0,sj} - d_{sj}\right) \hat{\boldsymbol{x}}_{sj}; \tag{2}$$

where N_s is the total number of *solid* particles connected to s, k_e is the spring constant normalised over the *smoothing length* (h), $d_{0,sj}$ and d_{sj} are the resting and current spring lengths, respectively, and $\hat{\boldsymbol{x}}_{sj} = \left(\boldsymbol{x}_s - \boldsymbol{x}_j\right)/d_{sj}$ is the unit vector directed from s to j. This total force is included in the momentum equations and thus integrated in the fractional-step scheme [73]. Specifically, it is added in the predictor-step equation as the mass force per unit mass. After calculating the updated velocity field, solid and fluid particles are moved at the end of each time step using the mean value of the new and old velocities.

The relationship between the spring constant and the Young's modulus was determined from uniaxial tensile tests simulations on a solid cube, as descripted in Monteleone *et al.* [73].

The pairs of *solid* particles linked by springs are defined at the beginning of the simulation (as shown in Figure 1a) and maintained throughout the analysis. Therefore, whilst the support domain of the fluid particles changes as a result of the particle movement (*i.e.* particles i_1, i_2, i_3 in a general configuration Figure 1b may have different neighbours from the reference state in Figure 1a), each *solid* particle maintains the same the list of neighbouring *solid* particles in all configurations.

2.2. The proposed benchmark test case

To validate the immersed FSI method, a new three-dimensional benchmark test case was devised. Figure 2 shows a 3D visualisation of the whole system (panel *a*) and a longitudinal cross-section with the dimensions of the model (panel *b*).

The system consists of a cylindrical tube terminated by a hemispherical end-cap (hereafter referred to as the hemisphere-capped cylinder, HCC, and highlighted in red in Figure 2b) made of an elastomeric deformable material, positioned coaxially around the nozzle at the distal end of a syringe. The cylindrical section of the HCC has an inner diameter of 20 mm and a constant wall thickness of 2 mm, while the hemispherical end-cap has the same inner diameter as the tube but a variable wall thickness, increasing from 2 mm at the junction to 3 mm at the distal tip of the dome. The CAD model in *initial graphics exchange specification* (*.iges*) format is provided in Supplementary 1.

To ensure optical access inside the HCC, the chamber was fabricated by injection molding, using Transil 40 silicone. This is a two-component platinum-cured RTV silicone rubber which, for thicknesses up to few millimetres, is optically clear.

The test fluid consisted of 75% propylene glycol (Carlo Erba Reagents) by volume, with the remaining 25% composed of phosphate-buffered saline (Sigma-Aldrich). This solution was specifically formulated to match the refractive index of the HCC material at room temperature, measured as n = 1.4095 using an Optika Abbe bench refractometer. The selected test fluid has density ρ_f =1.0445 g/ml and dynamic viscosity μ_f = 0.013478 Pa·s, measured using a Peak Hold test on a Discovery Hybrid Rheometer HR10 (TA Instruments, New Castle, DE, USA) at a shear rate of 10 s^{-1}, employing a stainless-steel conical geometry with a diameter of 60 mm and an angle of 2.016°. Since the HCC structure has inner and outer curved walls, the silicone chamber was enclosed within an external box with flat, transparent, parallel windows filled with the test fluid, in order to minimise optical distortions [94], [95]. The external box was 3D printed in black resin (Formlab) and closed with acrylic windows. A pipe, connected to an open tank exposed to the atmosphere, was incorporated to allow fluid to freely enter and exit the box, thereby accommodating the volume changes of the HCC. Figure 3 illustrates the deviation from rectilinear projection of a regular grid placed behind the external box–HCC system when filled with water (panel *a*) and with the test fluid (panel *b*). The results clearly show that the selected setup effectively eliminates optical distortion, restoring the grid pattern.

The syringe, with an internal diameter of 16 mm, was operated by a syringe pump in cyclic reciprocating motion with a triangular waveform. The forward plunger stroke produced a 25% volume increase in the HCC (1.883 ml) over 5 seconds, corresponding to a flow rate of 22.60 ml/min; the return stroke used the same flow rate. To account for plunger seal elasticity, manufacturing tolerances, and syringe pump response, the effective syringe motion was measured experimentally by tracking the plunger flange with a camera using the *vision.PointTracker* algorithm in MATLAB. This yielded a period of T = 10.476 s and an effective flow rate of Q = 27.62 ml/min. Detailed syringe motion data are provided in Supplementary 2 for reproducibility.

The liquid injected into the HCC induces a variation in the volume contained inside the chamber, and the presence of the central nozzle is expected to generate a vortex ring during the ejection.

Despite its simplicity, the system exhibits features common to complex cardiovascular models, such as large 3D strains of wall structures made from hyperelastic incompressible materials as effect of the interaction with dynamically pulsatile fluid flows.

The proposed benchmark was analysed experimentally using particle image velocimetry (PIV) and modelled using the proposed immersed fluid–structure interaction (FSI) method. Despite the

three-dimensional nature of both the experimental and numerical models, results comparison was conducted on a 2D diametral plane. This simplification is effective considering that the test case is axisymmetric. Accordingly, a 2D-PIV measurements was performed on the same diametral plane from which the FSI numerical results were analysed.

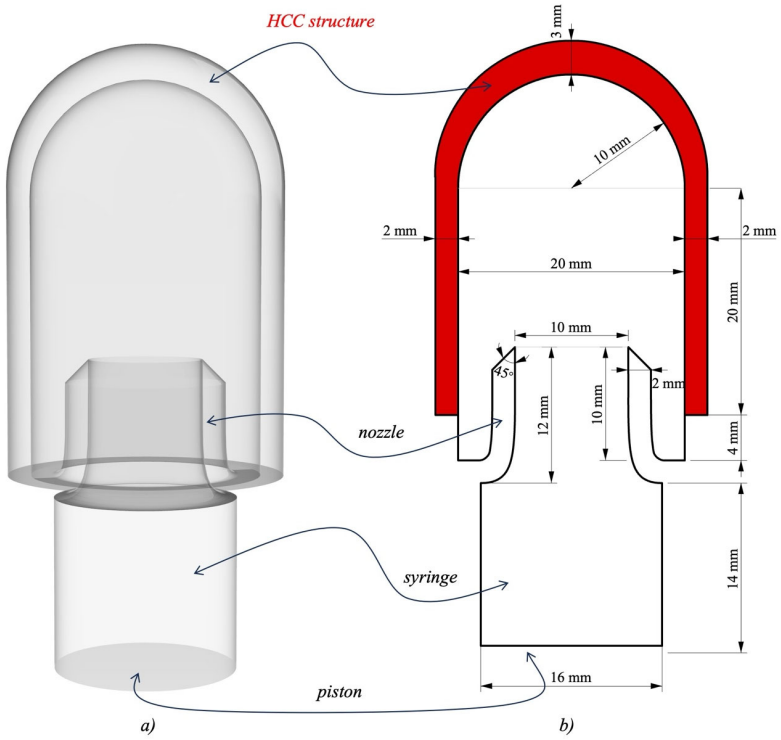

Figure 2: Benchmark test: a) 3D visualisation; b) longitudinal cross-section of the geometry with dimensions.

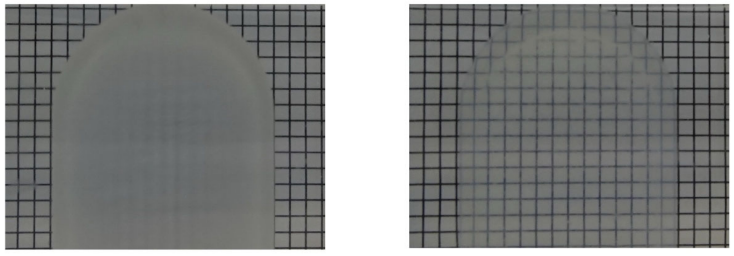

Figure 3: Refractive index mismatch between the HCC model made in Transil 40 silicone and a) water; b) 75 % propylene glycol solution.

2.3. PIV analysis

Experimental analysis of the proposed benchmark was conducted using phase resolved 2D-PIV, a non-intrusive optical technique that allows to capture velocity information of the whole flow field [96]. In brief, the fluid is seeded with small tracer particles, that are illuminated in a plane of interest with a laser sheet and acquired in couples of images captured in rapid succession with a high-speed camera. The images in each couple are then compared using cross-correlation algorithms, determining the flow parameters across the entire region of interest.

The experimental setup described above and used for the test is sketched in Figure 4.

Neutrally buoyant hollow glass spheres, 10 μm in diameter, where used to seed the fluid in the HCC chamber and syringe. Unseeded solution was used to fill the external box (through the red stopcock in Figure 4a) to ensure continuous refractive index matching. This outer fluid could flow into an external open chamber exposed to the atmosphere (see syringe at the top of Figure 4a), to allow free HCC expansion.

PIV test was performed using a 2D phase-resolved TSI system, composed of a double-pulse Nd:YAG laser of 300 mW and wavelength of 532 nm, and a CCD camera with 2048 × 2048 square pixels and frame rate of 15 Hz. The laser was connected to a collimator and a cylindrical lens of 15 mm, converting the laser beam into a light sheet approximately 1 mm thick. Camera and laser were synchronised with a laser-pulse synchronizer. The experiment was run projecting the laser sheet orthogonal to an external box window, along a sagittal symmetry plane of the HCC. The camera was placed orthogonal to the laser sheet, facing one of the adjacent external box windows. A photographic view of the experimental setup is provided in Figure 4b.

While the syringe pump was operating, 208 pairs of PIV images were acquired each 0.2 s in the Insight 4G software, with a time step $\Delta t = 0.05$ s between couples of images. These settings allow to capture three complete cycles, with over 50 image pairs per cycle.

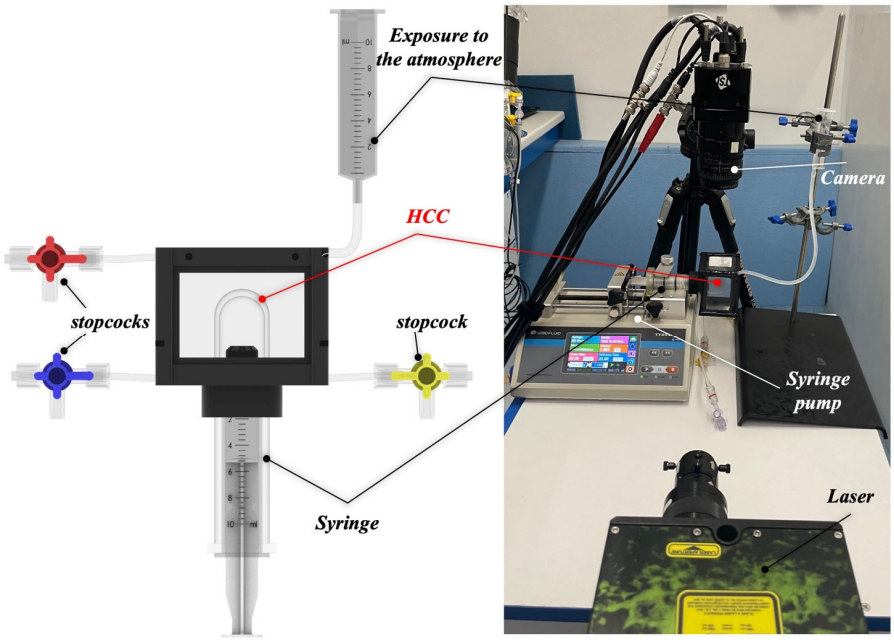

Figure 4: a) Sketch of the experimental model; b) PIV setup.

PIV images were processed using Insight 4G. After spatial calibration, a mask was applied to define the region of interest. A standard PIV algorithm was employed with the *image deformation* plugin, using the *fast Fourier transform* as the correlation engine and a *Gaussian peak* estimator [97]. The input images were first divided into interrogation regions (IRs) of 64 × 64 pixels to obtain an initial vector field. In a subsequent step, each IR was refined to 32 × 32 pixels and deformed to improve vector accuracy. Post-processing included a sequence of local validation steps and vector conditioning to ensure data quality. During local validation, vectors within a 5 × 5 IR neighborhood were compared to identify valid and invalid vectors. In the vector conditioning step, invalid vectors were removed and recursively replaced and smoothed using the surrounding valid vectors.

The resulting flow maps were then selected at characteristic time instants, for comparison with corresponding numerical solutions.

2.4. Numerical setup

In the numerical simulation, the fluid was modelled as incompressible and Newtonian, with a density and dynamic viscosity as determined for the experimental liquid (described in section 2.3).

Figure 5 shows a scheme of the system with the different SPH particle types and the employed boundary conditions. As discussed in section 2.1, the computational domain is defined larger than the effective domain dimensions (dimensions are provided in Figure 2), so as to include a buffer volume of particles (*reservoir fluid* particles displayed as grey circles in Figure 5) maintaining the deforming structure within the CRoI. The fluid domain, which includes the syringe and the liquid volume within the HCC, is filled by *effective fluid* particles (depicted as blue dots in Figure 5). *Solid*

particles occupy the region of the deformable HCC structure (red dots in Figure 5). An enlargement of the boxed region at the base of the HCC describes the boundary condition at the fixed region of the deformable structure. To this end, a flange of fixed *solid* particles (represented as empty red circles in Figure 5) is defined, where the position is maintained throughout the simulation. For the fluid domain, adherence boundary condition with null velocity (black continuous lines) is imposed at fixed walls (syringe and nozzle walls). The displacement of the syringe (orange curve in the graph of Figure 5), measured in the experimental test (see section 2.3), is imposed at the syringe plunger using adherence condition with moving boundary (orange line in the sketch of Figure 5).

A constant null pressure value is imposed at the open boundary of the buffer domain (dotted black line), allowing *reservoir fluid* particles to enter/exit allowing the structure deformation following the procedure described in Monteleone *et al.* [80].

In the simulation, a *smoothing length*, h, equal to 0.4 mm is used, corresponding to an initial total number of particles equal to 453,214 (subdivided as 187,793; 84,616;180,805; for the fluid, the structure and the buffer domains, respectively). This value was selected based on a particle-resolution study, considering three smoothing lengths (0.67 mm, 0.5 mm and 0.4 mm). Given the small differences in structural wall displacement and velocity profiles, h = 0.4 mm was chosen to maintain a particle density consistent with the PIV experiment. To ensure stability within the explicit integration scheme, the time step was determined by two primary constraints. First, it satisfied the Courant-Friedrichs-Lewy (CFL) condition for SPH: $\Delta t_{CFL} \leq \lambda_v (h/u_{max})$, where u_{max} is the maximum particle velocity magnitude and $\lambda_v = 0.4$ [98]. Additionally, the time step was limited by the maximum force magnitude experienced by the springs (f_{max}), defined as: $\Delta t_f \leq \lambda_f \left(\sqrt{h/f_{max}}\right)$ [99,100], where λ_f is a constant factor set equal to 0.25 [98,100]. Based on these conditions, a time step Δt = 0.002 s was employed in the simulation. Three consecutive piston strokes were performed, verifying that the periodicity was reached at the second cycle.

The simulation was carried out on an AMD EPYC GHz processor with 2 sockets and 24 cores per sockets. The CPU wall-clock time spent to advance the solution in time in serial mode is about 32 s (46.5 hours are thus required to simulate a whole period with the employed time step). Future development will be aimed at reducing computational costs, extending the parallelisation algorithm of Monteleone *et al.* [101].

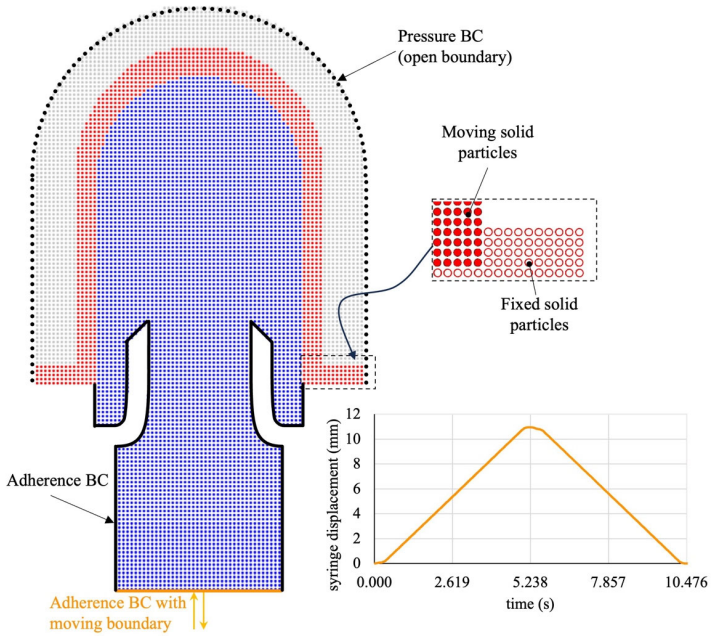

Figure 5: Sketch of the boundary conditions and SPH particle types in the proposed HCC benchmark (at the undeformed reference configuration). Blue dots: effective fluid particles; red dots: deformed solid particles; white dots with black contour: fixed solid particles; grey dots: reservoir fluid particles.

3. *Results and Discussion*

Four characteristics time instants were selected to analyse and compare numerical and experimental results in terms of fluid velocity and structural deformation. Specifically, the bottom dead centre (BDC), the top dead centre (TDC) and two intermediate instants at middle of the forward and return strokes were selected. The numerical results were analysed at the second cycle, as it was verified that the periodicity had already been reached.

Figure 6 shows the experimental and numerical velocity maps (left and right columns, respectively) at the analysed instants. Velocity vectors are represented in white, with constant length. For clarity, the velocity scale used at the dead centres (Figure 6a,c), when the flow inversion is associated with slower flow dynamics, range between 0 and 1.5 mm/s; whilst the instant at half strikes, characterised by faster motion (Figure 6b,d), are represented in a velocity scale ranging from 0 to 5 mm/s and when it proceeds with constant velocity.

At the BDC (see Figure 6a), the velocity is maximum at the exit of the nozzle, and drop close to the HCC wall. This region is characterised by the lowest velocities observed during the cycle, and is therefore associated with the largest experimental errors [102,103]. Moreover, the clear vortex ring observed in the numerical results is only partially visible in the PIV analysis due to its proximity to the lower mask edges.

During the forward stroke (see Figure 6b), fluid is pushed into the HCC, which expands. At this instant, velocity vectors are significantly higher in magnitude and reversed in direction with respect to the BDC instant, showing a fast jet at the nozzle exit progressively reducing towards the chamber walls.

At the TDC (see Figure 6c) both numerical and experimental maps show velocity peak of about 1.5 mm/s still directed towards the hemisphere, but now above the nozzle (where the mean velocity becomes negligible). This is accompanied by a concentric vortex ring, clearly observable in both studies.

In the return stroke (see Figure 6d), the velocity fields exhibit characteristics analogous to the respective forward case (see Figure 6b), but with inverted the vectors direction (these are now directed towards the nozzle), and slightly flatter in magnitude, a consequence of the increased fluidic resistance encountered during the passage of the flow from the HDC volume into the nozzle.

The velocity maps presented in Figure 6 demonstrate close agreement between experimental and numerical outcomes.

To enable a more quantitative comparison, velocity profiles were extracted at all analysed instants along a diameter located 6 mm above the nozzle, corresponding to the centre of the vortex ring generated at TDC (Figure 6c). The resulting profiles are shown in Figure 7. The experimental standard uncertainty of the selected velocity profile was evaluated at a 68% confidence level, representing the interval within which the true velocity values are expected to lie [97,104]. The mean standard uncertainty bound of each profile was compared with the mean velocity magnitude in the central 50% of the velocity profiles. The uncertainty bound of the velocity profiles resulted in the range 4-16% of the mean velocity magnitude.

Excellent agreement was observed between the numerical and experimental curves across all instants, with the maximum percentage difference of 11%, occurring at mid return stroke (Figure 7d). This value was calculated as the mean absolute relative error of the numerical result with respect to the experimental data within the central 50% of the velocity profiles.

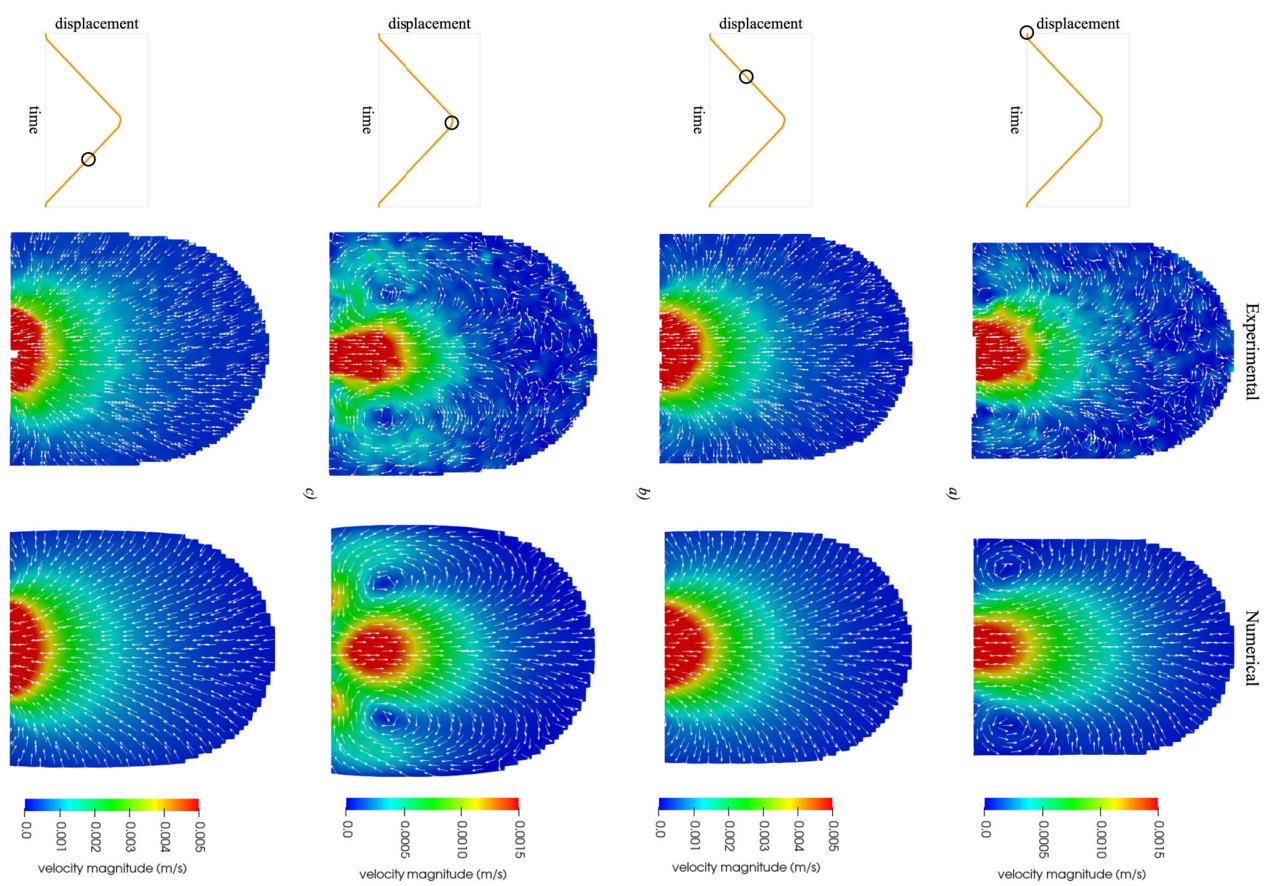

Figure 6: Experimental (left column) and numerical (right column) velocity maps at four time instants: a) minimum stroke; b) half stroke forward, c) direction inversion at the maximum stroke; d) half stroke back.

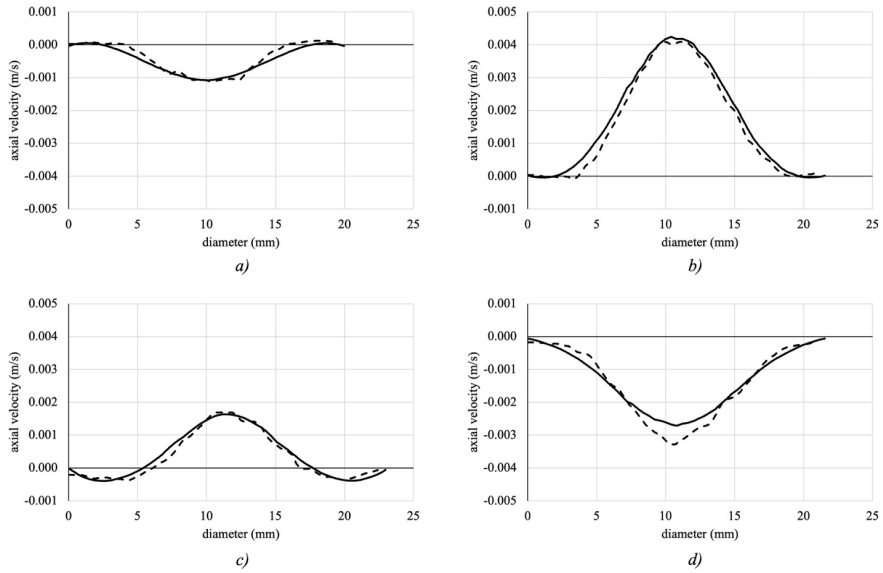

Figure 7: Comparison of velocity profile between experimental (dashed lines) and numerical (continuous lines) results at four time instants: a) minimum stroke; b) half stroke forward, c) inversion at the maximum stroke; d) half stroke back.

Furthermore, the deformation of the HCC walls was assessed. Figure 8 shows the solid particles (red dots) superimposed on the raw PIV images at the selected instants. As the HCC volume increases by 25%, the numerically predicted wall deformation closely matches the experimental observations at all instants, confirming excellent agreement. The video of the numerical results vs. experimental images of one cycle is made available in Supplementary 3.

The diameter variation (ΔD/D) measured at the midpoint of the HCC cylindrical region (see Figure 9a) is reported in Figure 9b, showing good agreement between experimental (dashed line) and numerical (solid line) results. Both experimental and computational outcomes achieve a peak variation of about 14 %, exhibiting a mean variation difference below 5%.

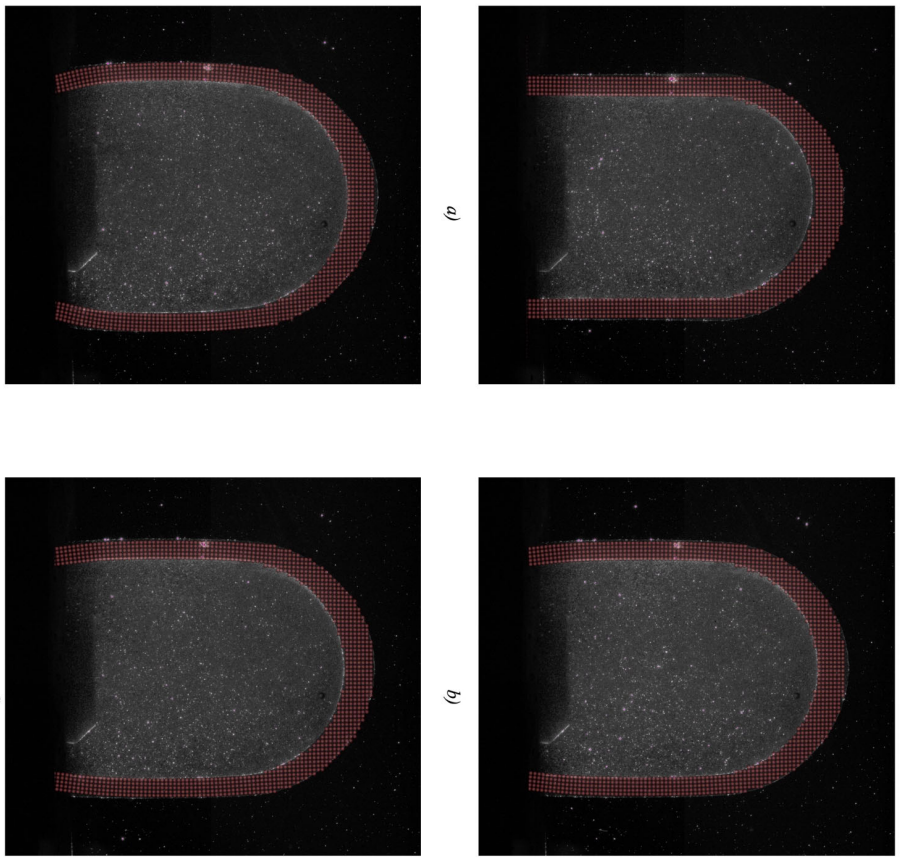

Figure 8: Comparison of the HCC deformation between experimental (PIV images) and numerical (red points) results at four time instants: a) minimum stroke; b) half stroke forward, c) inversion at the maximum stroke; d) half stroke back.

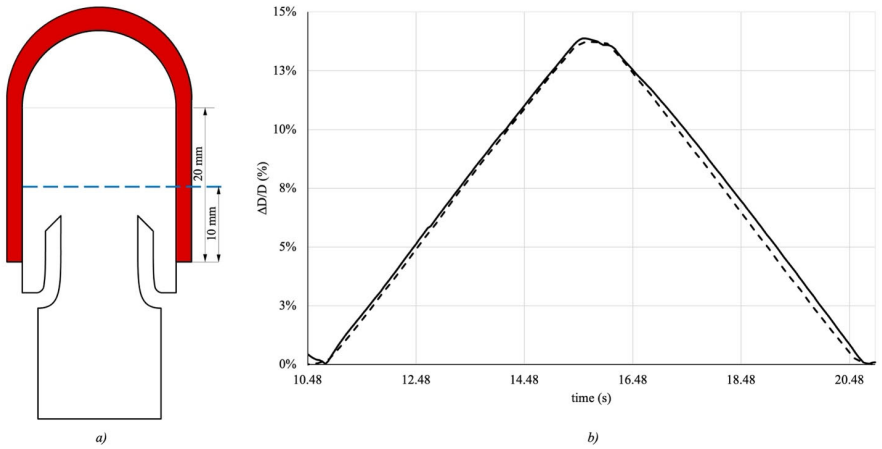

Figure 9: a) Longitudinal cross-section of the geometry with indication of the location of the diameter measurement (dashed blue line); b) comparison of the HCC diameter variation (ΔD/D) during the second cycle. Experimental (dashed line) and numerical (continuous line) results.

The proposed benchmark, simple to implement both experimentally and numerically, successfully reproduced a highly deformable chamber with curved walls interacting with a pulsatile flow. The resulting flow field was characterised by the formation of vortex rings during flow reversals (see Figure 6a,c), a hydrodynamic feature valuable for quantitative experimental validations. This setup therefore provides a simplified yet representative emulation of haemodynamic conditions occurring in complex cardiovascular scenarios, such as the filling and emptying of the left atrial appendage - an anatomical protrusion of the left atrium extensively investigated through computational approaches due to its elevated thromboembolic risk [8,34,105–108].

This benchmark may then serve as a practical reference for validating computational methods in cardiovascular scenarios, which are often assessed by comparison with other numerical approaches [109–112].

The proposed immersed FSI approach proved highly effective in simulating these scenarios, as demonstrated by the strong agreement between numerical and experimental results (Figure 6-Figure 9). A key advantage of the proposed method lies in its fully meshless nature, which eliminates the need for explicit FSI interface definitions and enables the use of a unified physical formulation for both fluid and solid phases. Within this framework, the shared fluid–structure computational domain prevents truncation of the kernel support and avoids particle penetration at the interface, without requiring additional corrective algorithms that would otherwise increase computational cost and methodological complexity. Crucially, this approach effectively addresses a longstanding challenge of boundary treatment in SPH methods, which often necessitates the introduction of mirror or ghost particles to enforce interface conditions [58,63,64,68,69].

The immersed FSI approach experimentally validated could be used in several cardiovascular applications characterised by complex patient-specific geometry and large deformation, *e.g.* to simulate the deformation of the left atrial appendage or the formation and effect of aneurysms.

Furthermore, the proposed FSI approach could be highly valuable in hybrid techniques, such as EMRI [85], which aim to correct 4D flow MRI data with numerical filtering. Its key advantage in this context is that it does not require any mesh definition or time dependent mesh updates, a major bottleneck for the application of such procedures to patient-specific geometries with moving walls [113].

Some limitations of the proposed FSI method should be noted. In particular, it requires the use of uniform discretisation for both fluid and structural domains, meaning that the modelling of thin structures dictates the choice of the *smoothing length* value, which can lead to large number of particles in specific problems. This issue, however, can be substantially mitigated employing procedures already implemented for the same code, such as parallelisation schemes [101] or multi-domain techniques [88]. Additionally, the material is modelled as incompressible, with density equal to that of the fluid, due to the employed ISPH approach. Although this assumption is effective for cardiovascular soft tissues [76,77] (and for elastomers such as the silicone employed in this study), it may not be applicable to synthetic biomaterials commonly used in prosthetic devices. The model is based on a basic description of the material constitutive laws, which currently does not model non-linearity, viscoelasticity, and anisotropy. The implementation of non-linear strain-energy responses, viscoelastic, and anisotropic behaviours represents a planned future development. A further concern is tensile instability, which induces particle clumping during computation and has consequently become one of the major barriers to the broader adoption of SPH in practical applications [92,93]. As mentioned in section 2.1, this work employs the shifting procedure proposed by Xu *et al.* [90] to ensure a more uniform particle distribution throughout the simulation. While this procedure mitigates the issue, tensile instability can still lead to numerical instability and unreliable results in long simulations (*e.g.*, if a large number of cycles are required to achieve periodicity). Moreover, although the shifting procedure is essential in ISPH simulation [114], it could introduce physical inaccuracies.

Moreover, as mentioned in the Introduction, the present approach was used to model thrombus formation, where convection-diffusion equations were included to model the evolution of biochemical species of the coagulative cascade [78,79]. These could be adapted in future studies including reaction terms to model electrophysiology effects.

4. Conclusions

An entirely meshless FSI approach is presented for modelling cardiovascular problems. The method is based on the ISPH algorithm, and uses a unified physics framework to represent both fluid and structure. Structure is handled linking SPH particles via spring laws, leading to an implicit FSI coupling since both fluid and solid particles are solved together in the same system. This overcomes a well-known FSI challenge related to the handling of fluid-solid interfaces. The absence of FSI interfaces is in fact a key advantage of this approach, making the method entirely meshless. This feature greatly simplifies the handling of large deformations and complex geometries inherent in cardiovascular simulations.

A key aspect of the present work is the rigorous experimental validation of the proposed FSI method. To this end, a novel benchmark test was introduced, designed to facilitate experimental validation while remining highly relevant for modelling complex cardiovascular phenomena. Despite

its simplified geometry, the benchmark captures essential features present in complex cardiovascular problems, including pulsatile flow, deformable curved walls, high three-dimensional strain and large volume variation during alternating filling and emptying phases. The experimental investigations were conducted using the PIV technique, widely recognised as the gold standard for in vitro flow analysis. Reference data of the benchmark, such as geometry, boundary conditions and experimental results are shared, to enable the scientific community to validate FSI computational approaches versus relevant experimental data.

The comparative analysis of numerical and experimental results demonstrated a very good match in both velocity fields and structural deformation. The experimentally validated FSI tool enable to obtain reliable numerical simulations in the cardiovascular framework, and could be use in future to provide deeper insights into blood and soft-tissues dynamic interaction and cardiovascular diseases.

Supplementary Material

Supplementary 1- Fluid and structural geometries of the FSI benchmark;
Supplementary 2- Experimental syringe displacement used as boundary condition of the numerical FSI benchmark;
Supplementary 3- Video of the numerical results vs. experimental images.

Acknowledgements

Part of this work was carried out with the financial support of the Regione Siciliana under the project 2021.IT.05.SFPR.014/002/04.7/09.02.03/A15_24/0001 (CIP), G71I24000280006 (CUP), DR 11689/2024.

Author Declarations

The authors have no conflicts to disclose.

Data availability statement

The data that supports the findings of this study are available within the article and its supplementary material.

References

[1] S. Schoenborn, S. Pirola, M.A. Woodruff, M.C. Allenby, Fluid-Structure Interaction Within Models of Patient-Specific Arteries: Computational Simulations and Experimental Validations, IEEE Rev. Biomed. Eng. 17 (2024) 280–296. https://doi.org/10.1109/RBME.2022.3215678.

[2] R. Pramanik, R.W.C.P. Verstappen, P.R. Onck, Computational fluid–structure interaction in biology and soft robots: A review, Physics of Fluids 36 (2024). https://doi.org/10.1063/5.0226743.

[3] O. Powar, P.A.H. Arun, A.M. Kumar, M. Kanchan, B.M. Karthik, P. Mangalore, M. Santhya, Recent Developments in the Immersed Boundary Method for Complex Fluid–Structure Interactions: A Review, Fluids 10 (2025) 134. https://doi.org/10.3390/fluids10050134.

[4] C.E.Jan.-L.E.A.-G.S.B.L.F.S.F.A.G.T.H.A.M.M. Bloom DE, The global economic burden of noncommunicable diseases. Program on the Global Demography of Aging, Program on the Global Demography of Aging, Number 8712 (2012).

[5] A. Athani, N.N.N. Ghazali, I.A. Badruddin, A.Y. Usmani, M. Amir, D. Singh, S.H. Khan, Image-Based Hemodynamic and Rheological Study of Patient's Diseased Arterial Vasculatures Using Computational Fluid Dynamics (CFD) and Fluid–Structure Interactions (FSI) Analysis: A review, Archives of Computational Methods in Engineering 32 (2025) 1427–1457. https://doi.org/10.1007/s11831-024-10193-5.

[6] M. Hirschhorn, V. Tchantchaleishvili, R. Stevens, J. Rossano, A. Throckmorton, Fluid–structure interaction modeling in cardiovascular medicine – A systematic review 2017–2019, Med. Eng. Phys. 78 (2020) 1–13. https://doi.org/10.1016/j.medengphy.2020.01.008.

[7] A.M. Tango, J. Salmonsmith, A. Ducci, G. Burriesci, Validation and Extension of a Fluid–Structure Interaction Model of the Healthy Aortic Valve, Cardiovasc. Eng. Technol. 9 (2018) 739–751. https://doi.org/10.1007/s13239-018-00391-1.

[8] G. Musotto, A. Monteleone, D. Vella, B. Zuccarello, R. Cannova, A. Cook, G.M. Bosi, G. Burriesci, Fluid-structure interaction analysis of the thromboembolic risk in the left atrial appendage under atrial fibrillation: Effect of hemodynamics and morphological features, Comput. Methods Programs Biomed. 246 (2024) 108056. https://doi.org/10.1016/j.cmpb.2024.108056.

[9] M.I. Afridi, M. Izadi, M. Eizadi, H.A. Mohammed, R. Karimi, F. Alqurashi, M.H. Mohamed, A. Hajjar, M.B. Ben Hamida, I. Mahariq, S. Rahimi, Fluid–structure interaction in engineering based on its applications: A plenary and up-to-date review, Physics of Fluids 36 (2024). https://doi.org/10.1063/5.0234435.

[10] K.D. Lau, V. Díaz-Zuccarini, P. Scambler, G. Burriesci, Fluid–structure interaction study of the edge-to-edge repair technique on the mitral valve, J. Biomech. 44 (2011) 2409–2417. https://doi.org/10.1016/j.jbiomech.2011.06.030.

[11] R. Jayendiran, B. Nour, A. Ruimi, Fluid-structure interaction (FSI) analysis of stent-graft for aortic endovascular aneurysm repair (EVAR): Material and structural considerations, J. Mech. Behav. Biomed. Mater. 87 (2018) 95–110. https://doi.org/10.1016/j.jmbbm.2018.07.020.

[12] J. De Hart, G.W.M. Peters, P.J.G. Schreurs, F.P.T. Baaijens, A three-dimensional computational analysis of fluid–structure interaction in the aortic valve, J. Biomech. 36 (2003) 103–112. https://doi.org/10.1016/S0021-9290(02)00244-0.

[13] A. Laadhari, G. Székely, Eulerian finite element method for the numerical modeling of fluid dynamics of natural and pathological aortic valves, J. Comput. Appl. Math. 319 (2017) 236–261. https://doi.org/10.1016/j.cam.2016.11.042.

[14] A.M. Tango, A. Ducci, G. Burriesci, In silico study of the ageing effect upon aortic valves, J. Fluids Struct. 103 (2021) 103258. https://doi.org/10.1016/j.jfluidstructs.2021.103258.

[15] A.P. Yoganathan, K.B. Chandran, F. Sotiropoulos, Flow in Prosthetic Heart Valves: State-of-the-Art and Future Directions, Ann. Biomed. Eng. 33 (2005) 1689–1694. https://doi.org/10.1007/s10439-005-8759-z.

[16] S.S. Abbas, M.S. Nasif, R. Al-Waked, State-of-the-art numerical fluid–structure interaction methods for aortic and mitral heart valves simulations: A review, Simulation 98 (2022) 3–34. https://doi.org/10.1177/00375497211023573.

[17] D. Oks, C. Samaniego, G. Houzeaux, C. Butakoff, M. Vázquez, Fluid–structure interaction analysis of eccentricity and leaflet rigidity on thrombosis biomarkers in bioprosthetic aortic valve replacements, Int. J. Numer. Method. Biomed. Eng. 38 (2022). https://doi.org/10.1002/cnm.3649.

[18] K.-M. Bornemann, S.E. Jahren, D. Obrist, The relation between aortic morphology and transcatheter aortic heart valve thrombosis: Particle tracing and platelet activation in larger aortic roots with and without neo-sinus, Comput. Biol. Med. 179 (2024) 108828. https://doi.org/10.1016/j.compbiomed.2024.108828.

[19] O. Mutlu, M. Saribay, M.M. Yavuz, H.E. Salman, A.R.D.M.H. Al-Nabti, H.C. Yalcin, Material modeling and recent findings in transcatheter aortic valve implantation simulations,

Comput. Methods Programs Biomed. 255 (2024) 108314. https://doi.org/10.1016/j.cmpb.2024.108314.

[20] A.M. Tango, A. Monteleone, A. Ducci, G. Burriesci, Analysis of the haemodynamic changes caused by surgical and transcatheter aortic valve replacements by means fluid-structure interaction simulations, Comput. Biol. Med. 186 (2025) 109673. https://doi.org/10.1016/j.compbiomed.2025.109673.

[21] M. Fandaros, C. Kwok, Z. Wolf, N. Labropoulos, W. Yin, Patient-Specific Numerical Simulations of Coronary Artery Hemodynamics and Biomechanics: A Pathway to Clinical Use, Cardiovasc. Eng. Technol. 15 (2024) 503–521. https://doi.org/10.1007/s13239-024-00731-4.

[22] A.A. Ekmejian, H.J. Carpenter, J.L. Ciofani, B.H.M. Gray, U.K. Allahwala, M. Ward, J. Escaned, P.J. Psaltis, R. Bhindi, Advances in the Computational Assessment of Disturbed Coronary Flow and Wall Shear Stress: A Contemporary Review, J. Am. Heart Assoc. 13 (2024). https://doi.org/10.1161/JAHA.124.037129.

[23] Y. He, H. Northrup, H. Le, A.K. Cheung, S.A. Berceli, Y.T. Shiu, Medical Image-Based Computational Fluid Dynamics and Fluid-Structure Interaction Analysis in Vascular Diseases, Front. Bioeng. Biotechnol. 10 (2022). https://doi.org/10.3389/fbioe.2022.855791.

[24] A.A. Rostam-Alilou, H.R. Jarrah, A. Zolfagharian, M. Bodaghi, Fluid–structure interaction (FSI) simulation for studying the impact of atherosclerosis on hemodynamics, arterial tissue remodeling, and initiation risk of intracranial aneurysms, Biomech. Model. Mechanobiol. 21 (2022) 1393–1406. https://doi.org/10.1007/s10237-022-01597-y.

[25] C. Zhao, R. Lv, A. Maehara, L. Wang, Z. Gao, Y. Xu, X. Guo, Y. Zhu, M. Huang, X. Zhang, J. Zhu, B. Yu, H. Jia, G.S. Mintz, D. Tang, Plaque Ruptures Are Related to High Plaque Stress and Strain Conditions: Direct Verification by Using In Vivo OCT Rupture Data and FSI Models, Arterioscler. Thromb. Vasc. Biol. 44 (2024) 1617–1627. https://doi.org/10.1161/ATVBAHA.124.320764.

[26] A. Balasubramanya, L. Gheysen, M.U. Wagenhäuser, N. Famaey, J. Degroote, P. Segers, Hemodynamics in aortic dissections: A fluid-solid interaction study in an idealized dissection model with a false lumen side branch, J. Biomech. 188 (2025) 112771. https://doi.org/10.1016/j.jbiomech.2025.112771.

[27] E.S. Di Martino, G. Guadagni, A. Fumero, G. Ballerini, R. Spirito, P. Biglioli, A. Redaelli, Fluid–structure interaction within realistic three-dimensional models of the aneurysmatic aorta as a guidance to assess the risk of rupture of the aneurysm, Med. Eng. Phys. 23 (2001) 647–655. https://doi.org/10.1016/S1350-4533(01)00093-5.

[28] M. Xenos, S.H. Rambhia, Y. Alemu, S. Einav, N. Labropoulos, A. Tassiopoulos, J.J. Ricotta, D. Bluestein, Patient-Based Abdominal Aortic Aneurysm Rupture Risk Prediction with Fluid Structure Interaction Modeling, Ann. Biomed. Eng. 38 (2010) 3323–3337. https://doi.org/10.1007/s10439-010-0094-3.

[29] J. Fonken, T. Timmer, A. Nievergeld, M. Thirugnanasambandam, M. van Sambeek, F. van de Vosse, R. Lopata, Longitudinal ultrasound-based fluid–structure interaction study on hemodynamics and wall mechanics in abdominal aortic aneurysms, Comput. Biol. Med. 195 (2025) 110486. https://doi.org/10.1016/j.compbiomed.2025.110486.

[30] A. Valencia, P. Burdiles, M. Ignat, J. Mura, E. Bravo, R. Rivera, J. Sordo, Fluid Structural Analysis of Human Cerebral Aneurysm Using Their Own Wall Mechanical Properties, Comput. Math. Methods Med. 2013 (2013) 1–18. https://doi.org/10.1155/2013/293128.

[31] R. Razaghi, H. Biglari, A. Karimi, Risk of rupture of the cerebral aneurysm in relation to traumatic brain injury using a patient-specific fluid-structure interaction model, Comput. Methods Programs Biomed. 176 (2019) 9–16. https://doi.org/10.1016/j.cmpb.2019.04.015.

[32] X. Wang, X. Huang, Risk factors and predictive indicators of rupture in cerebral aneurysms, Front. Physiol. 15 (2024). https://doi.org/10.3389/fphys.2024.1454016.

[33] A.K. Alagan, C. Valeti, S. Bolem, O.S. Karve, K.R. Arvind, P. Rajalakshmi, A. Sabareeswaran, S. Gopal, G. Matham, H.R. Darshan, B.J. Sudhir, B.S.V. Patnaik, Histopathology-based near-realistic arterial wall reconstruction of a patient-specific cerebral aneurysm for fluid-structure interaction studies, Comput. Biol. Med. 185 (2025) 109579. https://doi.org/10.1016/j.compbiomed.2024.109579.

[34] G. Musotto, A. Monteleone, D. Vella, S. Di Leonardo, A. Viola, G. Pitarresi, B. Zuccarello, A. Pantano, A. Cook, G.M. Bosi, G. Burriesci, The Role of Patient-Specific Morphological Features of the Left Atrial Appendage on the Thromboembolic Risk Under Atrial Fibrillation, Front. Cardiovasc. Med. 9 (2022). https://doi.org/10.3389/fcvm.2022.894187.

[35] K.K.L. Wong, P. Thavornpattanapong, S.C.P. Cheung, J. Tu, Numerical Stability of Partitioned Approach in Fluid-Structure Interaction for a Deformable Thin-Walled Vessel, Comput. Math. Methods Med. 2013 (2013) 1–10. https://doi.org/10.1155/2013/638519.

[36] A. Cetin, M. Sahin, A monolithic fluid-structure interaction framework applied to red blood cells, Int. J. Numer. Method. Biomed. Eng. 35 (2019). https://doi.org/10.1002/cnm.3171.

[37] S.T. Ha, L.C. Ngo, M. Saeed, B.J. Jeon, H. Choi, A comparative study between partitioned and monolithic methods for the problems with 3D fluid-structure interaction of blood vessels, Journal of Mechanical Science and Technology 31 (2017) 281–287. https://doi.org/10.1007/s12206-016-1230-2.

[38] A.G. Kuchumov, V. Vedeneev, V. Samartsev, A. Khairulin, O. Ivanov, Patient-specific fluid–structure interaction model of bile flow: comparison between 1-way and 2-way algorithms, Comput. Methods Biomech. Biomed. Engin. 24 (2021) 1693–1717. https://doi.org/10.1080/10255842.2021.1910942.

[39] D. Forti, M. Bukac, A. Quaini, S. Canic, S. Deparis, A Monolithic Approach to Fluid–Composite Structure Interaction, J. Sci. Comput. 72 (2017) 396–421. https://doi.org/10.1007/s10915-017-0363-5.

[40] J. Donea, S. Giuliani, J.P. Halleux, An arbitrary lagrangian-eulerian finite element method for transient dynamic fluid-structure interactions, Comput. Methods Appl. Mech. Eng. 33 (1982) 689–723. https://doi.org/10.1016/0045-7825(82)90128-1.

[41] M. Souli, A. Ouahsine, L. Lewin, ALE formulation for fluid–structure interaction problems, Comput. Methods Appl. Mech. Eng. 190 (2000) 659–675. https://doi.org/10.1016/S0045-7825(99)00432-6.

[42] E. Kuhl, S. Hulshoff, R. de Borst, An arbitrary Lagrangian Eulerian finite-element approach for fluid-structure interaction phenomena, Int. J. Numer. Methods Eng. 57 (2003) 117–142. https://doi.org/10.1002/nme.749.

[43] C.S. Peskin, The immersed boundary method, Acta Numerica 11 (2002) 479–517. https://doi.org/10.1017/S0962492902000077.

[44] I. Borazjani, Fluid–structure interaction, immersed boundary-finite element method simulations of bio-prosthetic heart valves, Comput. Methods Appl. Mech. Eng. 257 (2013) 103–116. https://doi.org/10.1016/j.cma.2013.01.010.

[45] B.E. Griffith, N.A. Patankar, Immersed Methods for Fluid–Structure Interaction, Annu. Rev. Fluid Mech. 52 (2020) 421–448. https://doi.org/10.1146/annurev-fluid-010719-060228.

[46] V.K. Srivastav, S. Thota, L.M. Kumar, A.R. Anand, Interface Problems-Fluid Structure Interaction: Description, Application and Review, WSEAS TRANSACTIONS ON BIOLOGY AND BIOMEDICINE 21 (2024) 218–226. https://doi.org/10.37394/23208.2024.21.22.

[47] F. Duarte, R. Gormaz, S. Natesan, Arbitrary Lagrangian–Eulerian method for Navier–Stokes equations with moving boundaries, Comput. Methods Appl. Mech. Eng. 193 (2004) 4819–4836. https://doi.org/10.1016/j.cma.2004.05.003.

[48] W. Mao, A. Caballero, R. McKay, C. Primiano, W. Sun, Fully-coupled fluid-structure interaction simulation of the aortic and mitral valves in a realistic 3D left ventricle model, PLoS One 12 (2017) e0184729. https://doi.org/10.1371/journal.pone.0184729.

[49] C. Ruan, J. Zhou, Z. Zhang, T. Li, L. Chen, Z. Li, Y. Chen, Numerical simulation progress of whole-heart modeling: A review, Physics of Fluids 36 (2024). https://doi.org/10.1063/5.0238853.
[50] C.S. Peskin, Flow patterns around heart valves: A numerical method, J. Comput. Phys. 10 (1972) 252–271. https://doi.org/10.1016/0021-9991(72)90065-4.
[51] G. Marom, Numerical Methods for Fluid–Structure Interaction Models of Aortic Valves, Archives of Computational Methods in Engineering 22 (2015) 595–620. https://doi.org/10.1007/s11831-014-9133-9.
[52] A.M. Bavo, G. Rocatello, F. Iannaccone, J. Degroote, J. Vierendeels, P. Segers, Fluid-Structure Interaction Simulation of Prosthetic Aortic Valves: Comparison between Immersed Boundary and Arbitrary Lagrangian-Eulerian Techniques for the Mesh Representation, PLoS One 11 (2016) e0154517. https://doi.org/10.1371/journal.pone.0154517.
[53] T.E. Tezduyar, S. Sathe, Modelling of fluid–structure interactions with the space–time finite elements: Solution techniques, Int. J. Numer. Methods Fluids 54 (2007) 855–900. https://doi.org/10.1002/fld.1430.
[54] A. Khayyer, H. Gotoh, Y. Shimizu, On systematic development of FSI solvers in the context of particle methods, Journal of Hydrodynamics 34 (2022) 395–407. https://doi.org/10.1007/s42241-022-0042-3.
[55] C. Antoci, M. Gallati, S. Sibilla, Numerical simulation of fluid–structure interaction by SPH, Comput. Struct. 85 (2007) 879–890. https://doi.org/10.1016/j.compstruc.2007.01.002.
[56] M. Liu, Z. Zhang, Smoothed particle hydrodynamics (SPH) for modeling fluid-structure interactions, Sci. China Phys. Mech. Astron. 62 (2019) 984701. https://doi.org/10.1007/s11433-018-9357-0.
[57] A. Zhang, P. Sun, F. Ming, A. Colagrossi, Smoothed particle hydrodynamics and its applications in fluid-structure interactions, Journal of Hydrodynamics 29 (2017) 187–216. https://doi.org/10.1016/S1001-6058(16)60730-8.
[58] C. Zhang, Y. Zhu, D. Wu, N.A. Adams, X. Hu, Smoothed particle hydrodynamics: Methodology development and recent achievement, Journal of Hydrodynamics 34 (2022) 767–805. https://doi.org/10.1007/s42241-022-0052-1.
[59] L.B. Lucy, A numerical approach to the testing of the fission hypothesis, Astron. J. 82 (1977) 1013. https://doi.org/10.1086/112164.
[60] R.A. Gingold, J.J. Monaghan, Smoothed particle hydrodynamics: theory and application to non-spherical stars, Mon. Not. R. Astron. Soc. 181 (1977) 375–389. https://doi.org/10.1093/mnras/181.3.375.
[61] M.B. Liu, G.R. Liu, Smoothed Particle Hydrodynamics (SPH): an Overview and Recent Developments, Archives of Computational Methods in Engineering 17 (2010) 25–76. https://doi.org/10.1007/s11831-010-9040-7.
[62] J.J. Monaghan, Smoothed Particle Hydrodynamics and Its Diverse Applications, Annu. Rev. Fluid Mech. 44 (2012) 323–346. https://doi.org/10.1146/annurev-fluid-120710-101220.
[63] G. Fourey, C. Hermange, D. Le Touzé, G. Oger, An efficient FSI coupling strategy between Smoothed Particle Hydrodynamics and Finite Element methods, Comput. Phys. Commun. 217 (2017) 66–81. https://doi.org/10.1016/j.cpc.2017.04.005.
[64] T. Long, D. Hu, D. Wan, C. Zhuang, G. Yang, An arbitrary boundary with ghost particles incorporated in coupled FEM–SPH model for FSI problems, J. Comput. Phys. 350 (2017) 166–183. https://doi.org/10.1016/j.jcp.2017.08.044.
[65] S.L. Fuchs, C. Meier, W.A. Wall, C.J. Cyron, A novel smoothed particle hydrodynamics and finite element coupling scheme for fluid–structure interaction: The sliding boundary particle approach, Comput. Methods Appl. Mech. Eng. 383 (2021) 113922. https://doi.org/10.1016/j.cma.2021.113922.
[66] S.M. Hosseini, J.J. Feng, A particle-based model for the transport of erythrocytes in capillaries, Chem. Eng. Sci. 64 (2009) 4488–4497. https://doi.org/10.1016/j.ces.2008.11.028.

[67] X. Yang, M. Liu, S. Peng, C. Huang, Numerical modeling of dam-break flow impacting on flexible structures using an improved SPH–EBG method, Coastal Engineering 108 (2016) 56–64. https://doi.org/10.1016/j.coastaleng.2015.11.007.
[68] G. Zhang, S. Wang, Z. Sui, L. Sun, Z. Zhang, Z. Zong, Coupling of SPH with smoothed point interpolation method for violent fluid-structure interaction problems, Eng. Anal. Bound. Elem. 103 (2019) 1–10. https://doi.org/10.1016/j.enganabound.2019.02.010.
[69] A. Monteleone, G. Borino, E. Napoli, G. Burriesci, Fluid–structure interaction approach with smoothed particle hydrodynamics and particle–spring systems, Comput. Methods Appl. Mech. Eng. 392 (2022) 114728. https://doi.org/10.1016/j.cma.2022.114728.
[70] C. Zhang, M. Rezavand, X. Hu, A multi-resolution SPH method for fluid-structure interactions, J. Comput. Phys. 429 (2021) 110028. https://doi.org/10.1016/j.jcp.2020.110028.
[71] A. Rafiee, K.P. Thiagarajan, An SPH projection method for simulating fluid-hypoelastic structure interaction, Comput. Methods Appl. Mech. Eng. 198 (2009) 2785–2795. https://doi.org/10.1016/j.cma.2009.04.001.
[72] A. Khayyer, H. Gotoh, H. Falahaty, Y. Shimizu, An enhanced ISPH–SPH coupled method for simulation of incompressible fluid–elastic structure interactions, Comput. Phys. Commun. 232 (2018) 139–164. https://doi.org/10.1016/j.cpc.2018.05.012.
[73] A. Monteleone, S. Di Leonardo, E. Napoli, G. Burriesci, A novel mono-physics particle-based approach for the simulation of cardiovascular fluid-structure interaction problems, Comput. Methods Programs Biomed. 245 (2024) 108034. https://doi.org/10.1016/j.cmpb.2024.108034.
[74] R. Gnyaneshwar, R.K. Kumar, K.R. Balakrishnan, Dynamic analysis of the aortic valve using a finite element model, Ann. Thorac. Surg. 73 (2002) 1122–1129. https://doi.org/10.1016/S0003-4975(01)03588-3.
[75] T. Ishihara, V.J. Ferrans, M. Jones, S.W. Boyce, O. Kawanami, W.C. Roberts, Histologic and ultrastructural features of normal human parietal pericardium, Am. J. Cardiol. 46 (1980) 744–753. https://doi.org/10.1016/0002-9149(80)90424-5.
[76] F. Di Puccio, S. Celi, P. Forte, Review of Experimental Investigations on Compressibility of Arteries and Introduction of a New Apparatus, Exp. Mech. 52 (2012) 895–902. https://doi.org/10.1007/s11340-012-9614-4.
[77] Y.C. Fung, Biomechanics: mechanical properties of living tissues, Springer Verlag, New York, 1993.
[78] A. Monteleone, A. Viola, E. Napoli, G. Burriesci, Modelling of thrombus formation using smoothed particle hydrodynamics method, PLoS One 18 (2023) e0281424. https://doi.org/10.1371/journal.pone.0281424.
[79] A.M. Lo Presti, A. Monteleone, G. Musotto, A. Tamburini, E. Napoli, G. Burriesci, Modelling of thrombus formation, growth and embolisation in the left atrial appendage under atrial fibrillation, Comput. Biol. Med. 191 (2025) 110134. https://doi.org/10.1016/j.compbiomed.2025.110134.
[80] A. Monteleone, M. Monteforte, E. Napoli, Inflow/outflow pressure boundary conditions for smoothed particle hydrodynamics simulations of incompressible flows, Comput. Fluids 159 (2017). https://doi.org/10.1016/j.compfluid.2017.09.011.
[81] J. Westerweel, G.E. Elsinga, R.J. Adrian, Particle Image Velocimetry for Complex and Turbulent Flows, Annu. Rev. Fluid Mech. 45 (2013) 409–436. https://doi.org/10.1146/annurev-fluid-120710-101204.
[82] F. Kojo Chaway Acquah, J. Paul Konadu Takyi, H.R. Beem, Design and characterization of a low-cost particle image velocimetry system, HardwareX 19 (2024) e00563. https://doi.org/10.1016/j.ohx.2024.e00563.
[83] M.D. Ford, H.N. Nikolov, J.S. Milner, S.P. Lownie, E.M. DeMont, W. Kalata, F. Loth, D.W. Holdsworth, D.A. Steinman, PIV-Measured Versus CFD-Predicted Flow Dynamics in

Anatomically Realistic Cerebral Aneurysm Models, J. Biomech. Eng. 130 (2008). https://doi.org/10.1115/1.2900724.
[84] H. Yang, I. Hong, Y.B. Kim, K.-C. Cho, J.H. Oh, Influence of blood viscosity models and boundary conditions on the computation of hemodynamic parameters in cerebral aneurysms using computational fluid dynamics, Acta Neurochir. (Wien). 165 (2023) 471–482. https://doi.org/10.1007/s00701-022-05467-5.
[85] G. Annio, R. Torii, A. Ducci, V. Muthurangu, V. Tsang, G. Burriesci, Experimental Validation of Enhanced Magnetic Resonance Imaging (EMRI) Using Particle Image Velocimetry (PIV), Ann. Biomed. Eng. (2021). https://doi.org/10.1007/s10439-021-02811-1.
[86] E. Napoli, M. De Marchis, E. Vitanza, PANORMUS-SPH. A new Smoothed Particle Hydrodynamics solver for incompressible flows, Comput. Fluids 106 (2015) 185–195. https://doi.org/10.1016/j.compfluid.2014.09.045.
[87] A.J. Chorin, Numerical solution of the Navier-Stokes equations, Math. Comput. 22 (1968) 745–762. https://doi.org/10.1090/S0025-5718-1968-0242392-2.
[88] A. Monteleone, M. De Marchis, B. Milici, E. Napoli, A multi-domain approach for smoothed particle hydrodynamics simulations of highly complex flows, Comput. Methods Appl. Mech. Eng. 340 (2018) 956–977. https://doi.org/10.1016/j.cma.2018.06.029.
[89] H.A. van der Vorst, H.A. van der Vorst, H.A. van der Vorst, Bi-CGSTAB: a fast and smoothly converging variant of Bi-CG for the solution of nonsymmetric linear systems, SIAM Journal on Scientific and Statistical Computing 13 (1992) 631–644. https://doi.org/10.1137/0913035.
[90] R. Xu, P. Stansby, D. Laurence, Accuracy and stability in incompressible SPH (ISPH) based on the projection method and a new approach, J. Comput. Phys. 228 (2009) 6703–6725. https://doi.org/10.1016/j.jcp.2009.05.032.
[91] J.W. Swegle, D.L. Hicks, S.W. Attaway, Smoothed Particle Hydrodynamics Stability Analysis, J. Comput. Phys. 116 (1995) 123–134. https://doi.org/10.1006/jcph.1995.1010.
[92] S. Liu, X. He, Y. Guo, Y. Chang, W. Wang, A Dual-Particle Approach for Incompressible SPH Fluids, ACM Trans. Graph. 43 (2024) 1–18. https://doi.org/10.1145/3649888.
[93] R. Vacondio, C. Altomare, M. De Leffe, X. Hu, D. Le Touzé, S. Lind, J.-C. Marongiu, S. Marrone, B.D. Rogers, A. Souto-Iglesias, Grand challenges for Smoothed Particle Hydrodynamics numerical schemes, Comput. Part. Mech. 8 (2021) 575–588. https://doi.org/10.1007/s40571-020-00354-1.
[94] R. Budwig, Refractive index matching methods for liquid flow investigations, Exp. Fluids 17 (1994) 350–355. https://doi.org/10.1007/BF01874416.
[95] S.F. Wright, I. Zadrazil, C.N. Markides, A review of solid–fluid selection options for optical-based measurements in single-phase liquid, two-phase liquid–liquid and multiphase solid–liquid flows, Exp. Fluids 58 (2017) 108. https://doi.org/10.1007/s00348-017-2386-y.
[96] M. Raffel, C.E. Willert, F. Scarano, C.J. Kähler, S.T. Wereley, J. Kompenhans, Particle Image Velocimetry, Springer International Publishing, Cham, 2018. https://doi.org/10.1007/978-3-319-68852-7.
[97] TSI, INSIGHT 4G, GLOBAL IMAGE, ACQUISITION, ANALYSIS, & DISPLAY SOFTWARE USER'S GUIDE (P/N 6004904, Revision E), TSI Incorporated, 2017.
[98] J.J. Monaghan, Smoothed Particle Hydrodynamics, Annu. Rev. Astron. Astrophys. 30 (1992) 543–574. https://doi.org/10.1146/annurev.aa.30.090192.002551.
[99] L., B.X., L.X., & W.X. He, Individual Time Stepping for SPH Fluids, Eurographics (Short Papers) (2015) 41–44.
[100] J., K.E. and M.T. Bender, Boundary handling and adaptive time-stepping for PCISPH, Workshop on Virtual Reality Interaction and Physical Simulation VRIPHYS 6 (2010).
[101] A. Monteleone, G. Burriesci, E. Napoli, A distributed-memory MPI parallelization scheme for multi-domain incompressible SPH, J. Parallel Distrib. Comput. 170 (2022) 53–67. https://doi.org/10.1016/j.jpdc.2022.08.004.

[102] M.G. Olsen, R.J. Adrian, Brownian motion and correlation in particle image velocimetry, Opt. Laser Technol. 32 (2000) 621–627. https://doi.org/10.1016/S0030-3992(00)00119-5.
[103] A. Sciacchitano, Uncertainty quantification in particle image velocimetry, Meas. Sci. Technol. 30 (2019) 092001. https://doi.org/10.1088/1361-6501/ab1db8.
[104] J.J. Charonko, P.P. Vlachos, Estimation of uncertainty bounds for individual particle image velocimetry measurements from cross-correlation peak ratio, Meas. Sci. Technol. 24 (2013) 065301. https://doi.org/10.1088/0957-0233/24/6/065301.
[105] A. Masci, L. Barone, L. Dedè, M. Fedele, C. Tomasi, A. Quarteroni, C. Corsi, The impact of left atrium appendage morphology on stroke risk assessment in atrial fibrillation: A computational fluid dynamics study, Front. Physiol. 9 (2019). https://doi.org/10.3389/fphys.2018.01938.
[106] D. Vella, A. Monteleone, G. Musotto, G.M. Bosi, G. Burriesci, Effect of the Alterations in Contractility and Morphology Produced by Atrial Fibrillation on the Thrombosis Potential of the Left Atrial Appendage, Front. Bioeng. Biotechnol. 9 (2021). https://doi.org/10.3389/fbioe.2021.586041.
[107] A.M. Lo Presti, A. Monteleone, G. Musotto, A. Tamburini, E. Napoli, G. Burriesci, Modelling of thrombus formation, growth and embolisation in the left atrial appendage under atrial fibrillation, Comput. Biol. Med. 191 (2025) 110134. https://doi.org/10.1016/j.compbiomed.2025.110134.
[108] L. Dedè, F. Menghini, A. Quarteroni, Computational fluid dynamics of blood flow in an idealized left human heart, Int. J. Numer. Method. Biomed. Eng. 37 (2019) e3287. https://doi.org/10.1002/cnm.3287.
[109] S. Turek, J. Hron, Proposal for Numerical Benchmarking of Fluid-Structure Interaction between an Elastic Object and Laminar Incompressible Flow, in: Fluid-Structure Interaction, Springer Berlin Heidelberg, Berlin, Heidelberg, n.d.: pp. 371–385. https://doi.org/10.1007/3-540-34596-5_15.
[110] S. Turek, J. Hron, M. Mádlík, M. Razzaq, H. Wobker, J.F. Acker, Numerical Simulation and Benchmarking of a Monolithic Multigrid Solver for Fluid-Structure Interaction Problems with Application to Hemodynamics, in: 2011: pp. 193–220. https://doi.org/10.1007/978-3-642-14206-2_8.
[111] A. Goetz, P.J. Rico, Y. Chau, J. Sédat, A. Larcher, E. Hachem, Proposal for Numerical Benchmarking of Fluid-Structure Interaction in Cerebral Aneurysms, (2023).
[112] R. Bhardwaj, R. Mittal, Benchmarking a Coupled Immersed-Boundary-Finite-Element Solver for Large-Scale Flow-Induced Deformation, AIAA Journal 50 (2012) 1638–1642. https://doi.org/10.2514/1.J051621.
[113] G. Annio, R. Torii, B. Ariff, D.P. O'Regan, V. Muthurangu, A. Ducci, V. Tsang, G. Burriesci, Enhancing Magnetic Resonance Imaging With Computational Fluid Dynamics, J. Eng. Sci. Med. Diagn. Ther. 2 (2019). https://doi.org/10.1115/1.4045493.
[114] M. Bagheri, M. Mohammadi, M. Riazi, A review of smoothed particle hydrodynamics, Comput. Part. Mech. 11 (2024) 1163–1219. https://doi.org/10.1007/s40571-023-00679-7.